CMS Physics Analysis Summary

Search for direct τ slepton pair production in proton-proton collisions at $\sqrt{s} = 13$ TeV

The CMS Collaboration

Abstract

A search for τ slepton pair production in proton-proton collisions at a center-of-mass energy of 13 TeV is presented. The data correspond to an integrated luminosity of 77.2 fb^{-1} collected with the CMS detector in 2016 and 2017. The search is carried out in events with a pair of τ leptons in the final state, expected from each τ slepton decaying into a τ lepton and a neutralino. We consider events in which both τ leptons decay hadronically, as well as events in which one of the τ leptons decays hadronically while the other decays to an electron or a muon. The observed data are consistent with the standard model background expectation, and the results are interpreted as upper limits on the cross section for τ slepton pair production in different scenarios. In the scenario of a purely left-handed τ slepton decaying to a nearly massless neutralino, the strongest limits are obtained for a τ slepton mass of 125 GeV, corresponding to 1.14 times the theoretical cross section.

1 Introduction

Supersymmetry (SUSY) [1–8] is an attractive extension of the standard model (SM) of particle physics, characterized by the presence of a superpartner for every SM particle. The superpartners have the same quantum numbers as their SM counterparts, except for spin, which is different by half a unit. One appealing feature of SUSY is that the cancellation of quadratic divergences in quantum corrections to the Higgs boson mass from SM particles and their superpartners could resolve the fine-tuning problem [9–14] affecting the SM. Another is that the lightest supersymmetric particle (LSP) is stable [15, 16] in SUSY models with R-parity conservation [17], and could be a dark matter (DM) candidate [18].

The hypothetical superpartner of the τ lepton, the τ slepton ($\widetilde{\tau}$), is the focus of the search reported in this paper. Supersymmetric models where the $\widetilde{\tau}$ is the next-to-lightest supersymmetric particle (NLSP) are well motivated in early universe $\widetilde{\tau}$-neutralino coannihilation scenarios, and could explain the observed DM relic density [19–24]. Such scenarios favor a light $\widetilde{\tau}$ with a relatively small mass splitting with the LSP. The existence of a light $\widetilde{\tau}$ would result in an enhanced probability of final states with τ leptons [25, 26].

In this analysis, we study simplified SUSY models [27–29] of direct $\widetilde{\tau}$ pair production, as shown in Fig. 1. We assume that the $\widetilde{\tau}$ decays to a τ lepton and $\widetilde{\chi}_1^0$, the lightest neutralino, which is assumed to be the LSP. The search is challenging because of the extremely small production cross section expected for this signal model. The most sensitive previous searches for direct $\widetilde{\tau}$ pair production were performed at the CERN LEP collider [30], excluding $\widetilde{\tau}$ masses of up to $\approx$90 GeV for neutralino masses of up to 80 GeV at 95% confidence level in some scenarios. At the CERN LHC, the ATLAS [31, 32] and CMS [33] Collaborations have both performed searches for direct $\widetilde{\tau}$ pair production with 8 TeV LHC data. CMS has previously carried out a search for direct $\widetilde{\tau}$ pair production with early 13 TeV data collected in 2016 [34]. In this paper, we present an update of this analysis incorporating the data collected in 2017. We study events with two τ leptons that may decay either hadronically or leptonically, and consider final states with either two hadronically decaying τ leptons (τ_h), or with one τ_h and an electron or a muon. These final states are denoted as the $\tau_h\tau_h$, $e\tau_h$, and $\mu\tau_h$ final states respectively. In this paper, we will refer to the analysis carried out in the $\tau_h\tau_h$ final state as the $\tau_h\tau_h$ analysis and the one carried out in the semileptonic ($e\tau_h$ and $\mu\tau_h$) final states as the $\ell\tau_h$ analysis. We have taken advantage of machine learning techniques to introduce two notable improvements in this version of the search, namely the incorporation of an improved τ_h selection method developed using a deep neural network (DNN) for the $\tau_h\tau_h$ analysis, and the use of a boosted decision tree (BDT) for event selection in the $\ell\tau_h$ analysis. There have also been improvements to the background estimation techniques and overall analysis structure.

We consider the superpartners of both left- and right-handed τ leptons, $\widetilde{\tau}_L$ and $\widetilde{\tau}_R$, respectively, in this paper. The cross section for $\widetilde{\tau}_L$ pair production is expected to be about three times larger than that for $\widetilde{\tau}_R$ pair production [35]. The experimental acceptance is also expected to be different between left- and right-handed scenarios because of differences in the polarization of the τ leptons produced in $\widetilde{\tau}$ decays. The decay products of hadronically (leptonically) decaying τ leptons originating from $\widetilde{\tau}_R$ decays would have larger (smaller) visible transverse momentum (p_T) than those originating from $\widetilde{\tau}_L$ decays. Two scenarios of direct $\widetilde{\tau}$ pair production are studied: one in which only $\widetilde{\tau}_L$ pairs are produced, and a degenerate scenario in which we assume that both $\widetilde{\tau}_L$ and $\widetilde{\tau}_R$ pairs are produced. No mixing is assumed between left- and right-handed states.
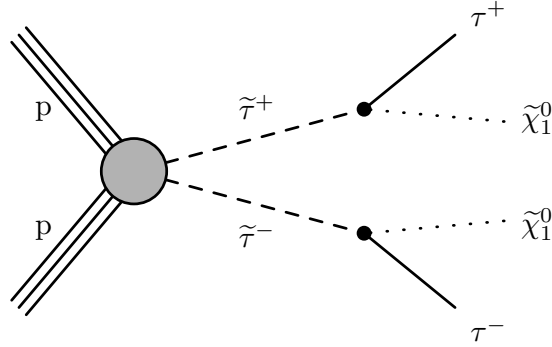
Figure 1: Diagram for direct $\widetilde{\tau}$ pair production followed by each $\widetilde{\tau}$ decaying to a τ lepton and a $\widetilde{\chi}_1^0$.

2 Event reconstruction and simulated samples

Event reconstruction uses a particle-flow (PF) algorithm [36], combining information from the tracker, calorimeter, and muon systems to identify charged and neutral hadrons, photons, electrons, and muons in an event. The missing transverse momentum, $\vec{p}_T^{\,\text{miss}}$, is computed as the negative vector sum of the p_T of all PF candidates reconstructed in an event, and its magnitude p_T^{miss} can be an important discriminator between signal and SM background. Events selected for the search are required to pass filters [37] designed to remove detector- and beam-related noise and must have at least one reconstructed vertex. Usually more than one such vertex is reconstructed, due to pileup, i.e., multiple proton-proton (pp) collisions within the same or neighboring bunch crossings. The mean number of interactions per bunch crossing was 23 in 2016, and increased to 32 in 2017. The reconstructed vertex with the largest value of summed physics-object p_T^2 is selected to be the primary pp interaction vertex. The physics objects are the jets, clustered using a jet finding algorithm [38, 39] with the tracks assigned to the vertex as inputs, and the $\vec{p}_T^{\,\text{miss}}$ calculated from those jets.

Charged particles that originate from the primary vertex, photons, and neutral hadrons are clustered into jets using the anti-k_T algorithm [38] with a distance parameter of 0.4, as implemented in the FASTJET package [39]. The jet energy is corrected to account for the contribution of additional pileup interactions in an event and to compensate for variations in detector response [39, 40]. In order to mitigate an issue related to noise in the electromagnetic calorimeter (ECAL) endcaps that led to significantly worse modeling of the p_T^{miss} distribution, particularly for events with large values of p_T^{miss} in 2017 data, jets in the region $2.65 < |\eta| < 3.139$ with uncorrected $p_T < 50\,\text{GeV}$ are removed from the $\vec{p}_T^{\,\text{miss}}$ calculation for 2017 data and simulation. This improves the agreement in the p_T^{miss} distribution between simulated events and data.

Jets considered in the search are required to have their axes within the tracker volume, in the range $|\eta| < 2.4$. For the $\tau_h\tau_h$ analysis, we count jets with $p_T > 30\,\text{GeV}$, while for the $\ell\tau_h$ analysis, we veto events containing jets with $p_T > 20\,\text{GeV}$ for more efficient background rejection. Jets are required to be separated by $\Delta R \equiv \sqrt{(\Delta\eta)^2 + (\Delta\phi)^2} > 0.4$ from electron, muon, or τ_h candidates that are selected for the analysis in order to avoid double counting of objects. Jets originating from the hadronization of b quarks are identified, or "tagged", with the combined secondary vertex (CSV) algorithm [41, 42]. The efficiency for tagging jets originating from b quarks is measured in simulated $t\bar{t}$ events to be about 63% for the working point used in the $\ell\tau_h$ analysis, while the misidentification rates for jets from charm quarks, and from light quarks or gluons, are about 12 and 0.9%, respectively. In the $\tau_h\tau_h$ analysis we use a version

of the CSV tagger developed using a DNN (DeepCSV), and a working point corresponding to an efficiency of 84% and misidentification rates of 41 and 11% for jets originating from charm quarks and light quarks or gluons, respectively.

Electron candidates are reconstructed by first matching clusters of energy deposited in the ECAL to reconstructed tracks. Selection criteria based on the distribution of the shower shape, track–cluster matching, and consistency between the cluster energy and track momentum are then used in the identification of electron candidates [43]. Muon candidates are reconstructed by requiring consistent measurement patterns in the tracker and muon systems [44]. We require the origin of electron and muon candidates to be consistent with the primary vertex. Restrictions are imposed on the magnitude of the impact parameters of their tracks with respect to the primary vertex in the transverse plane (d_{xy}), and on the longitudinal displacement (d_z) of those impact points. To ensure that an electron or muon candidate is isolated from any jet activity, the relative isolation quantity (I_{rel}), defined as the ratio of the scalar p_T sum of the particles in an η–ϕ cone around the candidate to the candidate p_T, is required to be below a threshold appropriate for the selection under consideration. An area-based estimate [40] of the pileup energy deposition in the cone is used to correct I_{rel} for contributions from particles originating from pileup interactions.

The τ_h candidates are reconstructed using the CMS hadron-plus-strips algorithm [45]. The constituents of the reconstructed jets are used to identify individual τ lepton decay modes with one charged hadron and up to two neutral pions, or three charged hadrons. The presence of extra particles within the jet, not compatible with the reconstructed decay mode, is used as a criterion to discriminate τ_h decays from other jets. A multivariate (MVA) discriminant, which contains isolation as well as lifetime information, is used to suppress the rate for quark and gluon jets to be misidentified as τ_h candidates. We employ a relaxed ("very loose") working point of this discriminant as a preselection requirement for the signal τ_h candidates selected in the $\tau_h\tau_h$ analysis, as well as in the extrapolation procedures used to estimate the contributions of events to the background in which quark or gluon jets are misidentified as τ_h. This working point corresponds to an efficiency of $\approx$70% for genuine τ_h, and a misidentification rate of $\approx$1% for quark or gluon jets. Two working points are used in the $\ell\tau_h$ analysis: "very tight" for selecting signal τ_h candidates, and "loose" in the extrapolation procedure used to estimate the misidentified τ_h background. These working points typically have efficiencies of around 40 and 57% for genuine τ_h, with a misidentification rate of approximately 0.01 and 0.04% for quark or gluon jets, respectively. Electrons and muons misidentified as τ_h are suppressed using dedicated criteria based on the consistency between the measurements in the tracker, calorimeters, and muon detectors [45].

The dominant background in the $\tau_h\tau_h$ final state originates from the misidentification of jets as τ_h. In order to further improve the suppression of this background while retaining high signal efficiency, we have pursued a new approach for improved τ_h isolation in the $\tau_h\tau_h$ analysis, based on the use of a DNN using the properties of PF candidates within an isolation cone ($\Delta R < 0.5$) around the τ_h candidate. We refer to this approach as the "Deep Particle Flow" (DeepPF) isolation. Charged PF candidates consistent with the PV, photon candidates, and neutral hadron candidates, with $p_T > 0.5$, 1, and 1.25 GeV, respectively, provide the inputs to the DeepPF isolation algorithm. The list of particle features incorporated for each candidate includes the candidate p_T relative to the τ_h jet, ΔR(candidate, τ_h), particle type, track quality information, d_{xy}, d_z, and the corresponding uncertainties, $\sigma(d_{xy})$ and $\sigma(d_z)$. A convolutional neural network is trained using simulated event samples, with signal τ_h candidates that are truth-matched to generator-level τ leptons from a mixture of processes that give rise to genuine τ leptons, and background candidates that fail the truth-matching taken from simulated

W+jets and QCD multijet event samples. The DNN output is averaged with the nominal MVA discriminant to obtain the final discriminator value for the optimal performance. The working point for the DeepPF isolation is chosen to maintain a flat efficiency of $\approx 50, 56$, and 56% vs p_T corresponding to the three reconstructed τ_h decay modes: one charged hadron, one charged hadron with neutral pions, and three charged hadrons, respectively. The overall misidentification rate for jets not originating from τ leptons ranges from 0.15 to 0.4%.

Significant contributions to the SM background for this search originate from Drell-Yan+jets (DY+jets), W+jets, $t\bar{t}$, and diboson processes, as well as from QCD multijet events. Smaller contributions arise from rare SM processes such as triboson and Higgs boson production, single top quark production, and top quark pair production in association with vector bosons. We rely on a combination of data control samples and Monte Carlo (MC) simulations to estimate the contributions of each background source. MC simulations are also used to model the signal processes.

The MADGRAPH5_aMC@NLO 2.3.3 (2.4.2) [46] event generator is used at leading order (LO) precision to produce simulated samples of the W+jets and DY+jets processes for the analysis of 2016 (2017) data. Top quark pair production, diboson and triboson production, and rare SM processes like single top production or top quark pair production with associated bosons, are generated at next-to-leading order (NLO) precision with MADGRAPH5_aMC@NLO and POWHEGv2 [47–50]. Showering and hadronization are carried out by the PYTHIA 8.205 (8.230) package [51] for the 2016 (2017) analysis, while a detailed simulation of the CMS detector is based on the GEANT4 [52] package. Finally, renormalization and factorization scale and PDF uncertainties have been derived with the use of the SYSCALC package [53]. Signal models of direct $\tilde{\tau}$ pair production are generated with MADGRAPH5_aMC@NLO at LO precision up to the production of τ leptons, which are then decayed with PYTHIA 8.212 for the samples used in the analysis of 2016 data, and PYTHIA 8.230 for those used in the analysis of 2017 data. For the 2016 analysis, the NNPDF3.0LO [54] set of parton distribution functions (PDFs) is used in generating W+jets, DY+jets, and signal samples, while the NNPDF3.0NLO set is used for other processes. The NNPDF3.1NLO set of PDFs is used for all samples for the 2017 analysis.

Event reconstruction in simulated samples is performed in a similar manner as for data. A nominal distribution of pileup interactions is used when producing the simulated samples. The samples are then reweighted to match the pileup profile observed in the collected data. We improve the modeling of initial-state radiation (ISR) in the signal simulated samples by reweighting the distribution of p_T^{ISR}, the total transverse momentum of the system of SUSY particles. This reweighting procedure is based on studies of the transverse momentum of Z boson events [55]. The signal production cross sections are calculated at NLO with next-to-leading logarithmic (NLL) soft-gluon resummation calculations [35]. The most precise cross section calculations that are available are used to normalize the SM simulated samples, corresponding most often to next-to-next-to-leading order (NNLO) accuracy.

3 Event selection

The data used for this search are selected with triggers that require the presence of isolated electrons, muons, τ_h candidates, or p_T^{miss}. The data used for the $\tau_h\tau_h$ analysis are selected with two sets of triggers. Events with $p_T^{miss} < 200\,\text{GeV}$ are selected with a trigger requiring the presence of two τ_h candidates, each with $p_T > 35\,(40)\,\text{GeV}$ in 2016 (2017). The di-τ_h trigger has a significant inefficiency for selecting signal events. We regain up to 7% signal efficiency for events with $p_T^{miss} > 200\,\text{GeV}$ with the help of a suite of p_T^{miss} triggers. For the $e\tau_h$ final state, the trigger used relies on the presence of an isolated electron with satisfying stringent

identification criteria and a p_T threshold of 25 (35) GeV in 2016 (2017). For the $\mu\tau_h$ final state, the trigger is based on the presence of an isolated muon with $p_T > 24$ (27) GeV in 2016 (2017). Trigger efficiencies are measured in data and simulation. We apply scale factors to account for any discrepancies to the simulation, parameterized in the p_T and η of the reconstructed electron, muon, or τ_h candidates, or of the reconstructed p_T^{miss} in the case of events selected through p_T^{miss} triggers.

3.1 Event selection and search region definition in the $\tau_h\tau_h$ final state

Subsequent to the trigger criteria, the baseline event selection requires the presence of exactly two isolated τ_h candidates of opposite charge satisfying the DeepPF selection described in Section 2, with $p_T > 40$ (45) GeV in 2016 (2017), and no additional τ_h candidates with $p_T > 30$ GeV satisfying the very loose working point of the MVA discriminant. We veto events with additional electrons or muons with $p_T > 20$ GeV and $|\eta| < 2.5$ (2.4) for electrons (muons), and reject any events with a b-tagged jet in order to suppress top quark related backgrounds. A requirement of $|\Delta\phi(\tau_{h1}, \tau_{h2})| > 1.5$ helps to suppress backgrounds originating from DY+jets and QCD multijet processes while retaining high signal efficiency. Finally, we require $p_T^{miss} > 50$ GeV in order to suppress the QCD multijet background.

The removal of low-p_T jets in the forward ECAL region from the $\vec{p}_T^{miss}$ calculation in 2017 in order to mitigate the effects of noise in this region improves the agreement between data and simulation. However, this also causes the background originating from DY+jets and other sources in the search sample to increase, since events with soft (low-p_T) jet activity in the forward ECAL region are assigned larger values of reconstructed p_T^{miss}. We offset some of the corresponding loss in sensitivity for the 2017 analysis by placing an upper bound of 50 GeV on the H_T (scalar p_T sum) of low-p_T jets excluded from the $\vec{p}_T^{miss}$ calculation. This restriction reduces the impact of background events with significant soft activity in the forward region for which the p_T^{miss} would be overestimated. A $Z \to \mu\mu$ control sample is used to derive correction factors for the soft forward H_T distribution in simulation to account for discrepancies with respect to the distribution observed in data, in order to ensure that the efficiency of this selection requirement is correctly estimated in simulation. Additionally, in order to avoid effects related to jet mismeasurement that can contribute to spurious p_T^{miss}, we require the $\vec{p}_T^{miss}$ to have a minimum separation of 0.25 in $|\Delta\phi|$ from jets with $p_T > 30$ GeV and $|\eta| < 2.4$, as well those with uncorrected $p_T > 50$ GeV in the region $2.4 < |\eta| < 3.139$.

Events satisfying the baseline selection criteria are subdivided into exclusive search regions (SRs) using several discriminating variables. In order to improve discrimination against the SM background, we take advantage of the expected presence of two $\tilde{\chi}_1^0$ in the final state for signal events, which would lead to additional p_T^{miss}. The correlations between $\vec{p}_T^{miss}$ and the reconstructed leptons are expected to be different between signal and background processes, even those with genuine p_T^{miss}, and these differences can be exploited. In particular, mass observables that can be calculated from the reconstructed leptons and the $\vec{p}_T^{miss}$ provide strong discriminants between signal and background. For a mother particle decaying to a visible and an invisible particle, the transverse mass (m_T), calculated using only the $\vec{p}_T$ of the decay products, should have a kinematic endpoint at the mass of the mother particle. Assuming that the p_T^{miss} corresponds to the p_T of the invisible particle, we calculate the m_T observable for the visible particle q and the invisible particle as follows:

$$m_T(q, \vec{p}_T^{miss}) \equiv \sqrt{2p_{T,q}p_T^{miss}(1 - \cos\Delta\phi(\vec{p}_{T,q}, \vec{p}_T^{miss}))}. \tag{1}$$

In this analysis we utilize the sum of the transverse mass between each τ_h and p_T^{miss}, $\Sigma m_T = m_T(\tau_{h1}, p_T^{miss}) + m_T(\tau_{h2}, p_T^{miss})$. Another variable found to be useful in the discrimination of signal against background is the "stransverse mass" m_{T2} [56–58]. This kinematic mass variable is a generalization of the variable m_T for situations with multiple invisible particles. It serves as an estimator of the mass of pair-produced particles in situations in which both particles decay to a final state containing the same invisible particle. For direct $\tilde{\tau}$ pair production, with both $\tilde{\tau}$ decaying to a τ lepton and a $\tilde{\chi}_1^0$, m_{T2} should be correlated with the mass difference between the $\tilde{\tau}$ and $\tilde{\chi}_1^0$. Large values of m_{T2} can therefore be used to discriminate between models with larger $\tilde{\tau}$ masses and the SM background. This variable is again calculated using the $\vec{p}_T$ of the different particles:

$$m_{T2} = \min_{\vec{p}_T^{X(1)} + \vec{p}_T^{X(2)} = \vec{p}_T^{miss}} \left[\max \left(m_T^{(1)}, m_T^{(2)} \right) \right], \quad (2)$$

where $\vec{p}_T^{X(i)}$ (with $i=1,2$) are the unknown transverse momenta of the two undetected particles and $m_T^{(i)}$ are the transverse masses obtained by pairing any of the two invisible particles with one of the two leptons. The minimization is done over the possible momenta of the invisible particles, assumed to be massless, which should add up to the $\vec{p}_T^{miss}$ in the event.

The SR selections for the $\tau_h \tau_h$ analysis, shown in Table 1, are based on a cut-and-count approach after applying the baseline selection. The regions are defined by selections on the following quantities: m_{T2}, Σm_T, and N_j (the number of reconstructed jets in an event). Distributions of Σm_T and m_{T2} after the baseline selection are shown in Fig. 2 for events in the $\tau_h \tau_h$ final state. In these and other distributions shown in this paper, the last bin includes overflows.

An initial selection of $m_{T2} > 25\,\text{GeV}$ is required for all SRs. After applying this minimum m_{T2} requirement, the Σm_T distribution is exploited to provide sensitivity towards a large range of $\tilde{\tau}$ mass signals. We define three bins in Σm_T: 200–250, 250–300, and >300 GeV. We then subdivide events in each Σm_T region into the following categories based on N_j: $N_j = 0$, and $N_j \geq 1$. This binning is highly beneficial as background events passing the SR kinematic selections are largely characterized by additional jet activity, while in the case of signal very few events have additional jets. The 0–jet category therefore provides us with nearly background-free SRs. However, we retain the SRs with $N_j \geq 1$ in order to avoid any loss of signal sensitivity from the presence of signal events in these SRs. Finally, events in each Σm_T and N_j region are further subdivided into low (25–50 GeV) and high (>50 GeV) m_{T2} regions, in order to improve sensitivity towards lower and higher $\tilde{\tau}$ mass signals, respectively.

Table 1: Ranges of m_{T2}, Σm_T, and N_j used to define the search regions used in the $\tau_h \tau_h$ analysis.

m_{T2} [GeV]	\> 50						25–50					
Σm_T [GeV]	\> 300		250–300		200–250		\> 300		250–300		200–250	
N_j	0	≥ 1	0	≥ 1	0	≥ 1	0	≥ 1	0	≥ 1	0	≥ 1

3.2 Event selection in the $\ell \tau_h$ final states

The baseline event selection for the $\ell \tau_h$ analysis requires either an electron with $p_T > 26$ (35) GeV with $|\eta| < 2.1$ or a muon with $p_T > 25$ (38) GeV and $|\eta| < 2.4$ for 2016 (2017) data, and a τ_h with p_T above 30 GeV and $|\eta| < 2.3$. For each of the reconstructed leptons, we require $|d_z| < 0.2\,\text{cm}$, and for the electron and muon we additionally require $|d_{xy}| < 0.045\,\text{cm}$. Electrons and muons have to satisfy $I_{rel} < 0.15$ and $I_{rel} < 0.1$, respectively. Backgrounds from $t\bar{t}$ and
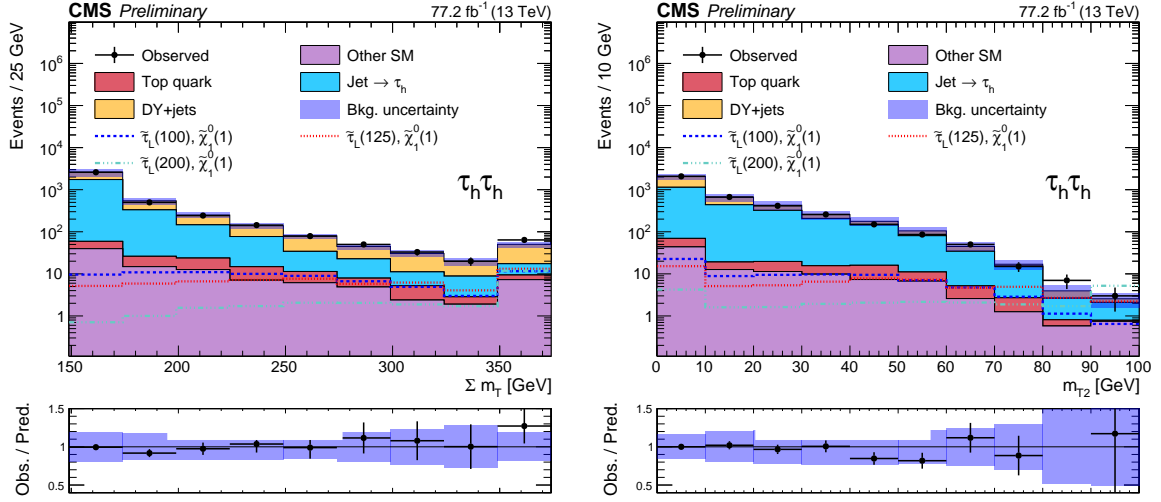
Figure 2: Distributions of Σm_T (left) and m_T2 (right) for events in the 2016 and 2017 datasets passing the baseline selection in the $\tau_\mathrm{h}\tau_\mathrm{h}$ final state, along with the corresponding prediction for the SM background and three benchmark signal models of $\widetilde{\tau}_\mathrm{L}$ pair production. The numbers within parentheses in the legend correspond to the masses of the $\widetilde{\tau}_\mathrm{L}$ and $\widetilde{\chi}_1^0$ in GeV. The shaded uncertainty band represents the statistical and systematic uncertainty in the background prediction.

W+jets are strongly reduced by vetoing events that contain jets with $p_\mathrm{T} > 20\,\mathrm{GeV}$. Events from W+jets are further reduced by requiring the transverse mass $m_\mathrm{T}(\ell, \vec{p}_\mathrm{T}^{\,\mathrm{miss}})$, calculated with the electron or muon momentum vector and $\vec{p}_\mathrm{T}^{\,\mathrm{miss}}$, to be between 20 and 60 GeV or above 120 GeV. Another significant background, from DY+jets events, is reduced by requiring the invariant mass of the electron or muon and the τ_h, $m(\ell\tau_\mathrm{h})$ to exceed 50 GeV. In order to reduce QCD multijet events, we require $2.0 < \Delta R(\ell, \tau_\mathrm{h}) < 3.5$.

With this preselection in place, we train several BDTs corresponding to different signal hypotheses to classify signal and background events. The following input variables are used: the electron or muon and τ_h p_T, $p_\mathrm{T}^{\mathrm{miss}}$, $m_\mathrm{T}(\ell, \vec{p}_\mathrm{T}^{\,\mathrm{miss}})$, $\Delta\eta(\ell, \tau_\mathrm{h})$, $\Delta\phi(\ell, \vec{p}_\mathrm{T}^{\,\mathrm{miss}})$ and $\Delta\phi(\tau_\mathrm{h}, \vec{p}_\mathrm{T}^{\,\mathrm{miss}})$, $\Delta R(\ell, \tau_\mathrm{h})$, $m_\mathrm{T}^{\mathrm{tot}} \equiv \sqrt{m_\mathrm{T}^2(\ell, \vec{p}_\mathrm{T}^{\,\mathrm{miss}}) + m_\mathrm{T}^2(\tau_\mathrm{h}, \vec{p}_\mathrm{T}^{\,\mathrm{miss}})}$, and $m(\ell\tau_\mathrm{h})$. We also include m_T2 and the contransverse mass [59, 60] computed from the visible decay products, defined as

$$m_\mathrm{CT} \equiv \sqrt{2 p_{\mathrm{T},\ell}\, p_{\mathrm{T},\tau_\mathrm{h}} (1 + \cos\Delta\phi(\ell, \tau_\mathrm{h}))}, \qquad (3)$$

which is expected to have an endpoint around $(m(\widetilde{\tau})^2 - m(\widetilde{\chi}_1^0)^2)/m(\widetilde{\tau})$ for signal events. Finally, we include $D_\zeta = \vec{p}_\mathrm{T}^{\,\mathrm{miss}} \cdot \vec{\zeta} - 0.85(\vec{p}^{\,\ell_1} + \vec{p}^{\,\ell_2}) \cdot \vec{\zeta}$, with $\vec{\zeta}$ being the bisector between the direction of the two leptons [61, 62]. The value of 0.85 has been optimized to efficiently distinguish DY+jets events from the other backgrounds and the signal. Figure 3 shows distributions of two of the BDT input variables, $p_\mathrm{T}^{\mathrm{miss}}$ and $m_\mathrm{T}^{\mathrm{tot}}$, for events passing the baseline selection in the $\mu\tau_\mathrm{h}$ final state. The distributions observed in the $\mathrm{e}\tau_\mathrm{h}$ final state are similar.

Since the signal kinematics depend on mass, we train BDTs for signals with different $\widetilde{\tau}$ masses: 100, 150, and 200 GeV, all with a $\widetilde{\chi}_1^0$ mass of 1 GeV. As the results of the training depend critically on the number of input events, we relax the τ MVA isolation criteria and reduce the τ_h p_T threshold to 20 GeV for the training sample in order to increase the number of training and test events. The nominal "very tight" isolation and τ_h p_T threshold of 30 GeV are applied when evaluating the BDT output for the analysis. For a given signal hypothesis, we choose the BDT trained with the same $\widetilde{\tau}$ mass in the case of models with $\widetilde{\tau}$ masses of 100, 150, and 200 GeV, or

the one that provides the optimal sensitivity in the case of models with other $\widetilde{\tau}$ masses. For signal models with $\widetilde{\tau}$ masses of 90 and 125 GeV, the BDT trained for $m(\widetilde{\tau}) = 100$ GeV is used, while for those with a $\widetilde{\tau}$ mass of 175 GeV, the BDT trained for $m(\widetilde{\tau}) = 200$ GeV is used. While signal events are largely expected to have high BDT output values, we use the full BDT distribution in the fit used for signal extraction.
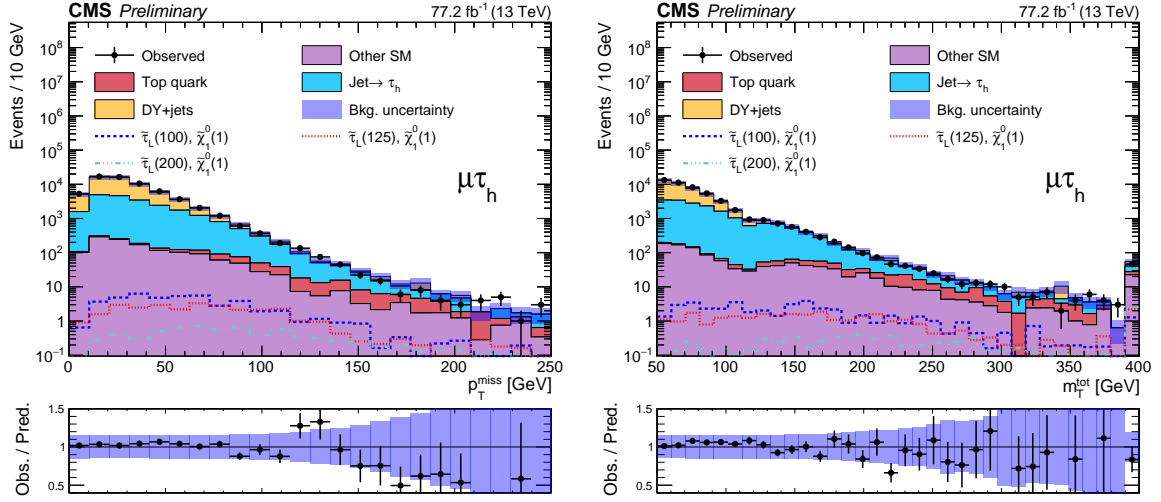

Figure 3: Distributions of p_T^{miss} (left) and m_T^{tot} (right) for events in the 2016 and 2017 datasets passing the baseline selection in the $\mu\tau_h$ final state, along with the corresponding prediction for the SM background and three benchmark signal models of $\widetilde{\tau}_L$ pair production. The numbers within parentheses in the legend correspond to the masses of the $\widetilde{\tau}_L$ and $\widetilde{\chi}_1^0$ in GeV. The shaded uncertainty band represents the statistical and average systematic uncertainty in the background prediction.

4 Background estimation

The most significant background sources for this search are DY+jets, W+jets, QCD multijet, $t\bar{t}$, and diboson processes. These background sources have different relative contributions in the different final states. For the $\tau_h\tau_h$ final state, the dominant background originates from QCD multijet and W+jets processes, where one or more of the τ_h candidates originates from a jet that is misidentified as a prompt τ_h. For the $\ell\tau_h$ final states, the main backgrounds after the baseline selection are DY+jets ($\approx$50%), W+jets ($\approx$30%), and QCD multijet ($\approx$10%) events. The DY+jets background contribution, which is also the second largest background in the $\tau_h\tau_h$ final state, usually consists of events with two prompt leptons. It is determined from simulation after applying shape and normalization corrections that are determined from data. The W+jets and QCD multijet backgrounds usually contain one or more jets misidentified as τ_h, and their contributions are determined using methods that rely on data. Finally we have smaller contributions from other SM backgrounds, like Higgs boson and diboson production and top quark pair production (with or without extra vector bosons). These are estimated from simulation, with appropriate correction factors applied. A detailed description of the procedures used to estimate the background contributions from the different sources follows.

4.1 Estimation of the background from misidentified jets

4.1.1 Estimation in the $\tau_h \tau_h$ final state

After requiring two high-p_T τ_h candidates, the dominant background for the search in the $\tau_h \tau_h$ final state consists of QCD multijet and W+jets events, in which one or both of the τ_h candidates originate from a jet and are misidentified as prompt τ_h. This background is predicted using a method relying on extrapolation from a data sample selected with a relaxed isolation requirement. We estimate how frequently nonprompt or misidentified τ_h candidates that are selected with the very loose MVA isolation working point also pass the tight analysis DeepPF isolation requirement applied in the SRs by studying a multijet-enriched control sample where we require both τ_h candidates to have the same charge. The same-charge di-τ_h event sample is collected with the same di-τ_h trigger as the search sample, in order to take into account any biases from the isolation requirement present at the trigger level, which is not identical to the analysis isolation requirement. We also require m_{T2} to be small ($< 40\,\text{GeV}$) to reduce any potential contributions from signal and W+jets events.

The final rate measured in this sample for misidentified τ_h selected with the very loose MVA isolation working point to pass the tight DeepPF isolation requirement is around 20%, but it depends considerably on the p_T and the decay mode (one- or three-prong) of the τ_h candidate, and the parent jet flavor. The misidentification rate is measured in bins of τ_h p_T and decay mode to reduce any dependence on these factors. The measurement is also binned in the number of primary vertices (N_{PV}) to capture the effects of pileup. A systematic uncertainty of around 30% is evaluated to account for the dependence of the misidentification rate on the jet flavor, based on studies performed in simulation.

Since the isolation efficiency for prompt τ_h candidates is only around 70-80%, processes with genuine τ_h may leak into the data sideband regions and need to be taken into account when calculating the final estimate for the background processes with misidentified τ_h. To take this correctly into account, we define three categories for events that have at least two loosely isolated τ_h candidates: events with both τ_h candidates passing the tight DeepPF isolation requirement, events with one passing and one failing the tight isolation requirement, and finally events with both τ_h candidates failing the tight isolation requirement. We then equate these observable quantities with the expected sum totals of contributions from events with two prompt τ_h candidates, two misidentified τ_h candidates, or one prompt and one misidentified τ_h candidate to each of these populations. The contributions of background events with one or two misidentified τ_h candidates in the SRs can then be determined analytically by inverting this set of equations.

4.1.2 Estimation in the $e\tau_h$ and $\mu\tau_h$ final states

The misidentification of jets as τ_h candidates also gives rise to a major source of background for the search in the $e\tau_h$ and $\mu\tau_h$ final states, mainly from W+jets events with leptonic W boson decays. We estimate this background from a sideband sample in data selected by applying the SR selections, with the exception that the τ_h candidates are required to satisfy the loose isolation working point, but not the very tight working point. A transfer factor for the extrapolation in τ_h isolation is determined from a W+jets control sample selected from events with one muon and at least one τ_h candidate that passes the loose isolation requirement. In events with more than one τ_h candidate, the most isolated candidate is used in the determination of the transfer factor. Events with additional electrons or muons satisfying looser criteria are rejected. In order to increase the purity of W+jets events in this sample by reducing the contribution of $t\bar{t}$ and QCD multijet events, we require $60 < m_T(\ell, p_T^{\text{miss}}) < 120\,\text{GeV}$, $p_T^{\text{miss}} > 40\,\text{GeV}$, no more than

two jets, and an azimuthal separation of at least 2.5 radians between any jet and the W boson reconstructed from the muon and the $\vec{p}_T^{\text{miss}}$. The remaining sample has an expected purity of 82% for W+jets events. The transfer factor, R, is then determined from this control sample, after subtracting the remaining non-W+jets background contributions estimated from simulation, as follows:

$$R = \frac{N_{\text{data}}^{\text{CS}}(\text{VT}) - N_{\text{MC no W}}^{\text{CS}}(\text{VT})}{N_{\text{data}}^{\text{CS}}(\text{L\&!VT}) - N_{\text{MC no W}}^{\text{CS}}(\text{L\&!VT})}. \tag{4}$$

Here, $N_{\text{data}}^{\text{CS}}$ corresponds to the number of events in the control sample in data. The parenthetical arguments VT and L&!VT denote events in which the τ_h candidate satisfies the very tight isolation working point, and those that do not satisfy it but do satisfy the loose requirement, respectively. The transfer factor is determined in bins of p_T and η of the τ_h candidate.

The contribution of the background originating from a jet misidentified as a τ_h candidate in the search sample is then determined from the corresponding data sideband region selected by requiring that the τ_h candidate satisfies the loose isolation requirement, but does not satisfy the very tight working point, as follows:

$$N(\text{jet} \rightarrow \tau) = R\left(N_{\text{data}}^{\text{sideband}} - N_{\text{MC}}^{\text{sideband}}(\text{genuine } \tau)\right), \tag{5}$$

where $N_{\text{data}}^{\text{sideband}}$ represents the number of data events in the sideband region, from which $N_{\text{MC}}^{\text{sideband}}(\text{genuine } \tau)$, the expected contribution of events with genuine τ leptons determined from simulation with generator-level matching, is subtracted. We validate the misidentified τ_h estimation using a control region with $60 < m_T(\ell, \vec{p}_T^{\text{miss}}) < 120\,\text{GeV}$ and an additional requirement of $\Delta\phi(\text{W,jet}) > 2.5$ to ensure that this region is fully orthogonal to the region described above that is used to estimate the background.

4.2 Estimation of the Drell–Yan+jets background

The DY+jets background mainly originates from $Z \rightarrow \tau\tau$ decays. We estimate the contribution of this background from simulation after corrections based on control samples in data. If the Z boson mass shape or p_T spectrum are poorly modeled in the simulation, then distributions of the discriminating kinematic variables can differ significantly between data and simulation, especially at the high-end tails that are relevant for the $\tau_h\tau_h$ SRs. We therefore use a high-purity $Z \rightarrow \mu\mu$ control sample to compare the dimuon mass and p_T spectra between data and simulation and apply the observed differences as corrections to the simulation in the search sample in the form of two-dimensional weights parameterized in the generator-level Z boson mass and p_T. The correction factors range up to 30% for high mass and p_T values. Since these correction factors are intended to compensate for missing higher-order effects in the simulation, we assign the difference between the generator-level Z boson mass and p_T shapes obtained from LO and NLO simulated samples as a systematic uncertainty. The known differences in the electron, muon, and τ_h identification and isolation efficiencies, jet, electron, muon, and τ_h energy scales, and b tagging efficiency between data and simulation are taken into account. The uncertainties corresponding to these corrections are also propagated to the final background estimate. The corrected simulation is validated in the $\tau_h\tau_h$ final state using a $Z \rightarrow \tau\tau$ control sample selected by inverting the m_{T2} and Σm_T requirements used to define the SRs. Additionally requiring a p_T of at least 50 GeV for the $\tau_h\tau_h$ system reduces the QCD multijet background and improves the purity of this control sample. The $p_T^{\text{miss}} > 50\,\text{GeV}$ requirement is removed as well. The distribution of the visible mass of the di-τ_h system shown in Fig. 4 (left) demonstrates that the corrected simulation agrees with the data within the experimental uncertainties in this sample.

For the analysis in the semileptonic final states, a normalization scale factor as well as corrections to the Z p_T distribution in the simulation are derived from a very pure $Z \rightarrow \mu\mu$ control

sample in data. Events in this sample are selected by requiring two isolated muons and no additional leptons, fewer than two jets, no b-tagged jets, and a dimuon mass window of 75–105 GeV to increase the probability that they originate from $Z \rightarrow \mu\mu$ decays to >99%. After subtracting all other contributions estimated from simulation, a normalization scale factor that is compatible with unity within its uncertainty is extracted from the ratio of data to simulated events. The uncertainty in the scale factor is dominated by the systematic uncertainty.

To validate the DY+jets background prediction in the $\ell\tau_h$ analysis, we construct a control sample with $m_T(\mu, E_T^{miss}) > 20$ GeV, $50 < m(\ell\tau_h) < 80$ GeV, and $N_j = 0$. The distribution of the visible mass of the $\mu\tau_h$ system in this sample is shown in Fig. 4 (right). Once again, we observe good agreement between data and the predicted background.
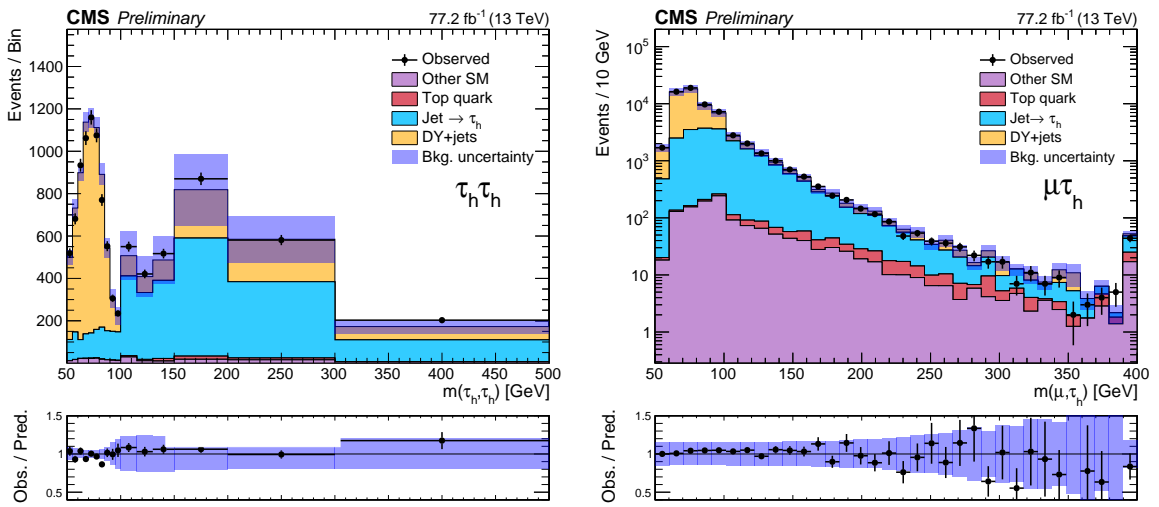

Figure 4: Visible mass spectrum of the τ lepton pair system in data and the corresponding prediction for the SM background for the combined 2016 and 2017 datasets for the $\tau_h\tau_h$ (left) and $\ell\tau_h$ (right) DY+jets validation samples. The shaded uncertainty band represents the statistical and systematic uncertainty in the background prediction. In the $\ell\tau_h$ case, the systematic uncertainty included in the band for each bin corresponds to a single average value. Agreement is observed within uncertainties in both cases.

4.3 Estimation of other backgrounds

Smaller contributions exist from other SM backgrounds, including diboson, triboson, and Higgs boson processes. There are also contributions from top quark processes: $t\bar{t}$ and single top quark production, or top quark pair production in association with vector bosons. These are estimated from simulation, using the known efficiency and energy scale corrections and evaluating both experimental and theoretical uncertainties as described in Section 5.

For the $\ell\tau_h$ analysis, a control region to test the BDT distribution in a $t\bar{t}$ enriched region is constructed by requiring the event selection to be the same as for the search region, except for the requirement of one or two b-tagged jets, while to validate the WW background prediction, we construct a control region with an oppositely charged muon-electron pair selection, $M_{\mu e} > 90$ GeV and $N_j = 0$. We derive systematic uncertainties for the normalization of the corresponding backgrounds and to account for any potential mismodeling of the BDT shape from our studies in these control regions.

5 Systematic uncertainties

The dominant uncertainties in this analysis are the statistical uncertainties, driven by the limited event counts in the data sidebands or simulated samples used to obtain the background estimates, and the systematic uncertainty in the fake rate estimate.

We rely on an extrapolation in the τ_h isolation to obtain an estimate of the background with misidentified τ_h candidates. In the $\tau_h\tau_h$ analysis, the uncertainty in this extrapolation is driven by the uncertainty introduced by the dependence of the isolation on the jet flavor. It also includes the statistical uncertainty in the control regions from which the extrapolation factors are measured. The uncertainty in the identification and isolation efficiency for prompt τ_h candidates is propagated to the final estimated uncertainty as well. In the $\ell\tau_h$ analysis, we estimate a transfer factor for the extrapolation in τ_h isolation from a W+jets control sample. The purity of this sample is $\approx$85%. We propagate the $\approx$15% contamination from other processes as a systematic uncertainty.

We use simulation to obtain estimates of the other background contributions and the signal yields. We propagate uncertainties related to the b tagging, trigger, and selection efficiencies, renormalization and factorization scale uncertainties, PDF uncertainties, and uncertainties in the jet energy scale, jet energy resolution, unclustered energy contributing to p_T^{miss}, and the energy scales of electrons, muons, and τ_h. For the DY+jets background, we have an additional uncertainty related to the corrections applied to the mass shape and p_T distribution. We assign a 15% normalization uncertainty in the $\tau_h\tau_h$ final state for the production cross sections of processes estimated from simulation based on CMS differential cross section measurements [63–65]. For the $\ell\tau_h$ analysis, we derive normalization uncertainties of 5, 5, and 20% for the DY+jets, $t\bar{t}$, and WW backgrounds, respectively, based on the purity of the corresponding control regions enriched in each process. An additional uncertainty of 9% is assigned to cover potential mismodeling of the BDT shape in simulation based on studies in the control regions.

The categorization of events in the $\tau_h\tau_h$ final state according to the number of reconstructed jets makes us sensitive to the modeling of ISR in the signal simulation. The p_T^{ISR} distribution of simulated signal events is reweighted to improve the ISR modeling, using reweighting factors derived from studies of Z boson events. We take the deviation of the reweighting factors from unity as a systematic uncertainty.

The uncertainty in the integrated luminosity measurement is taken into account in all background estimates for which we do not derive normalization scale factors in dedicated data control samples, as well as for signal processes. This uncertainty corresponds to 2.5% and 2.3% for the 2016 [66] and 2017 [67] datasets respectively. The main systematic uncertainties for the signal models and background estimates are summarized in Table 2.

In general we treat all statistical uncertainties as uncorrelated, while systematic uncertainties related to the same modeling effect are taken to be correlated across the different background and signal predictions. Between the 2016 and 2017 data analyses, all uncertainties deriving from statistical limitations are uncorrelated. Systematic uncertainties derived from similar sources are treated as correlated or partially correlated. For the combination of the $\tau_h\tau_h$ and $\ell\tau_h$ analyses, we correlate uncertainties related to object reconstruction, with the exception of the τ_h selection efficiency, which is treated as uncorrelated between the two analyses due to the use of different isolation algorithms.

Table 2: Systematic uncertainties in the analysis for the different SM background predictions and for a representative signal model, corresponding to a left-handed $\widetilde{\tau}$, with $m(\widetilde{\tau}) = 100\,\text{GeV}, m(\widetilde{\chi}_1^0) = 1\,\text{GeV}$. The uncertainty values are relative to the corresponding event yields in different search regions and are listed as percentages.

Uncertainty (%)	Signal	Misidentified τ_h	DY+jets	Top quark	Other SM
τ_h efficiency	5–13	—	5–15	1–14	10–51
e/μ efficiency ($\ell\tau_h$)	2–3	—	2–3	2–3	2–3
τ_h energy scale	0.5–12	—	2.6–27	1.2–11	4.1–13
e/μ energy scale ($\ell\tau_h$)	0.1–25	0.1–5	0.1–30	0.1–20	0.1–10
Jet energy scale	0.5–38	—	1.1–19	0.6–13	2.4–14
Jet energy resolution	0.3–22	—	1.9–10	0.7–22	0.2–11
Unclustered energy	0.3–21	—	2.6–30	0.2–6.4	1.7–14
B–tagging	0.2–0.9	—	0.2–23	1.7–25	0.2–1.2
Pileup	0.9–9.1	—	2–22	0.1–24	0.3–25
BDT shape ($\ell\tau_h$)	9	—	9	9	9
$\ell \to \tau_h$ misidentification rate ($\ell\tau_h$)	—	—	—	1	1
Integrated luminosity	2.3–2.5	—	2.3	2.3	2.3–2.5
Background normalization	—	10	5–15	2.5–15	15–25
Drell–Yan mass and p_T	—	—	0.2–11	—	—
τ_h misidentification rate	—	4.6–51	—	—	—
Signal ISR	0.2–8.2	—	—	—	—
Renormalization/factorization scale	1.6–7	—	0.7–14	0.7–30	6.7–16
PDF	—	—	0.1–1.2	0.1–0.4	0.1–0.6

6 Results and interpretation

The results of the search in the $\tau_h\tau_h$ final state are presented in Fig. 5 and summarized in Tables 3-4. Distributions of the BDT trained for a $\widetilde{\tau}$ mass of 100 GeV and a $\widetilde{\chi}_1^0$ mass of 1 GeV are shown before and after the maximum likelihood fit to the data in Fig. 6 for the $\mu\tau_h$ final state. The data is well described by the prediction for the SM background. The predicted and observed event yields in the last BDT bins, which are the most sensitive to signal, are summarized in Tables 5-6 for the $\ell\tau_h$ final states. For the statistical interpretation of these results, normalization uncertainties affecting background and signal predictions are generally assumed to be log normal distributed. In the case of statistical uncertainties driven by small event counts in data or simulation samples, a gamma distribution is used.

The results are interpreted as limits on the cross section for the production of $\widetilde{\tau}$ pairs in the context of simplified models [27–29, 68] using all the exclusive $\tau_h\tau_h$ search regions and the shapes of the $\ell\tau_h$ BDT distributions in a full statistical combination. We assume that the $\widetilde{\tau}$ decays with 100% branching fraction to a τ lepton and a $\widetilde{\chi}_1^0$. The 95% confidence level (CL) upper limits on SUSY production cross sections are calculated using a modified frequentist approach with the CL_s criterion [69, 70] and asymptotic results for the test statistic [71, 72]. Figure 7 shows the limits obtained in the scenario of purely left-handed $\widetilde{\tau}$ pair production, while Fig. 8 shows the limits obtained for the degenerate $\widetilde{\tau}$ scenario, in which we assume that both left- and right-handed $\widetilde{\tau}$ pairs are produced. The strongest limits are observed in the case of a nearly massless $\widetilde{\chi}_1^0$. In general, the constraints are reduced for higher values of the $\widetilde{\chi}_1^0$ mass, due to smaller experimental acceptances. In the purely left-handed scenario, the strongest limits are observed for a $\widetilde{\tau}$ mass of 125 GeV when assuming a nearly massless $\widetilde{\chi}_1^0$. In this model we exclude a $\widetilde{\tau}$ pair production cross section of 132 fb, which is 1.14 times the theoretical cross section. In the degenerate $\widetilde{\tau}$ scenario, we exclude $\widetilde{\tau}$ masses between 90 and 150 GeV under assumption of a nearly massless $\widetilde{\chi}_1^0$.
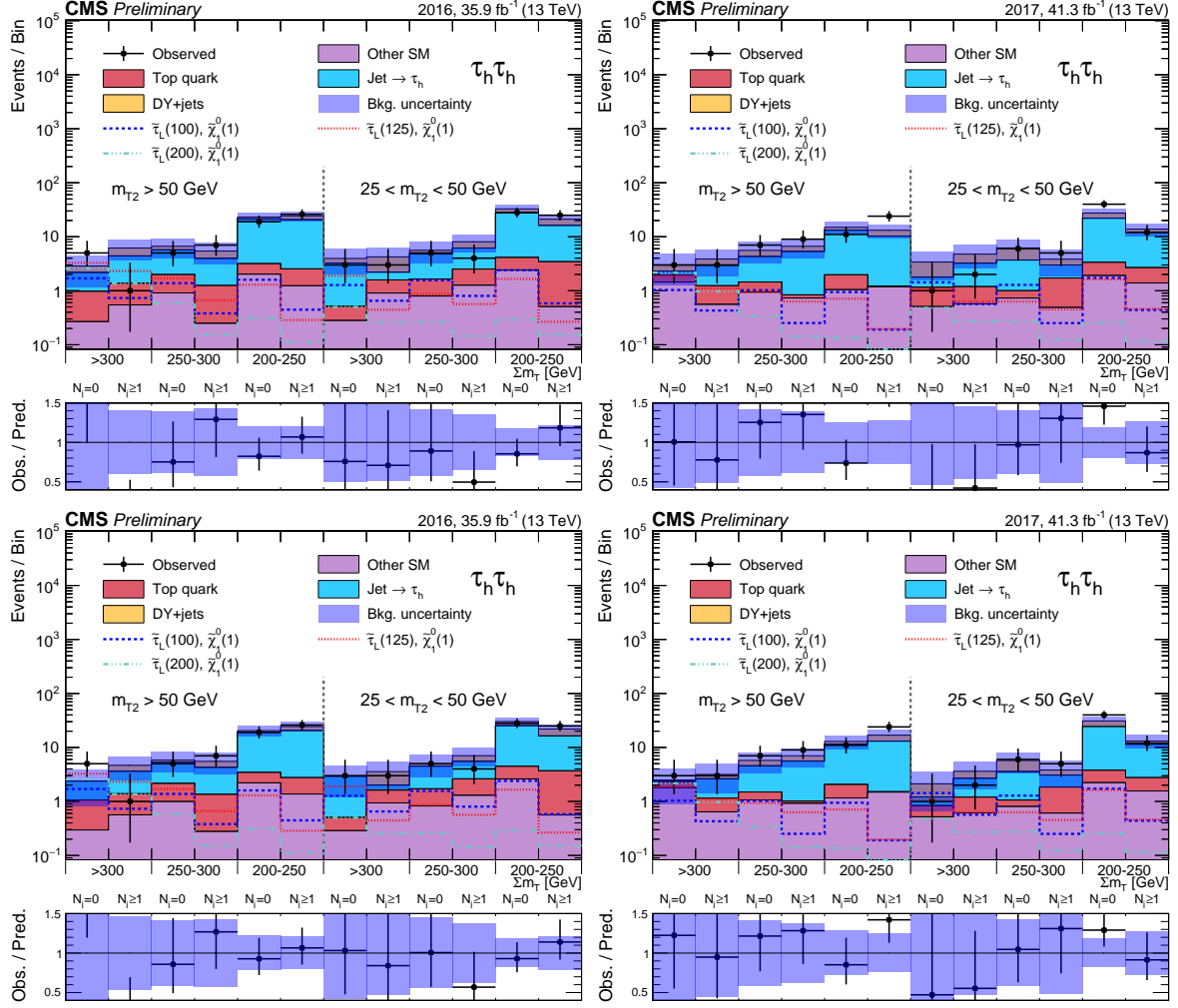
Figure 5: Observed event counts and predicted yields for the SM background in the $\tau_h \tau_h$ analysis for the 2016 (left) and 2017 (right) datasets, before (top) and after (bottom) the maximum likelihood fit to the data. Predicted signal yields are also shown for benchmark signal models with $m(\tilde{\tau}) = 100, 125,$ and $200\,\text{GeV}$, $m(\tilde{\chi}_1^0) = 1\,\text{GeV}$.

7 Summary

A search for direct τ slepton ($\tilde{\tau}$) pair production has been performed in proton-proton collisions at a center-of-mass energy of 13 TeV in events with a τ lepton pair and significant missing transverse momentum. Search regions are defined using discriminating kinematic observables that exploit expected differences between signal and background. The data sample used for this search corresponds to an integrated luminosity of $77.2\,\text{fb}^{-1}$ collected in 2016 and 2017. No excess above the expected standard model background has been observed. Upper limits on the cross section of direct $\tilde{\tau}$ pair production are derived for simplified models in which each $\tilde{\tau}$ decays to a τ lepton and the lightest neutralino, with the latter being assumed to be the lightest supersymmetric particle (LSP). In the scenario of purely left-handed $\tilde{\tau}$ pair production, the analysis is most sensitive to a $\tilde{\tau}$ mass of 125 GeV when the neutralino is nearly massless. The observed limit is 1.14 times the expected production cross section in this simplified model. The limits observed in this scenario are the strongest obtained thus far for $\tilde{\tau}$ masses above 100 GeV. For a more optimistic, degenerate production scenario, in which both left- and right-handed $\tilde{\tau}$ pairs are produced, we exclude $\tilde{\tau}$ masses up to 150 GeV when assuming a nearly massless

Table 3: Predicted background yields and observed event counts in all $\tau_h\tau_h$ SRs, corresponding to 35.9 fb^{-1} of data collected in 2016. For the background estimates with no events in the sideband or the simulated sample, the 68% statistical upper limit is taken. The uncertainties listed in quadrature are statistical and systematic respectively. We also list the predicted signal yields corresponding to the purely left-handed scenario for a $\widetilde{\tau}$ mass of 100 GeV and a $\widetilde{\chi}_1^0$ mass of 1 GeV.

m_{T2} [GeV]	> 50					
Σm_T [GeV]	> 300		250 − 300		200 − 250	
N_j	0	≥ 1	0	≥ 1	0	≥ 1
Misidentified τ_h	1.1 ± 0.6 ± 0.6	2.9 ± 0.8 ± 1.6	3.7 ± 1.0 ± 2.2	2.7 ± 1.1 ± 0.5	18.2 ± 2.8 ± 9.5	18.1 ± 2.9 ± 6.0
DY+jets	< 0.7	1.3 ± 0.8 ± 0.5	0.5 ± 0.5 ± 0.1	1.0 ± 0.7 ± 0.1	1.1 ± 0.8 ± 0.2	3.3 ± 1.3 ± 0.7
Top quark	0.7 ± 0.2 ± 0.1	0.8 ± 0.2 ± 0.1	1.1 ± 0.2 ± 0.2	1.0 ± 0.2 ± 0.1	1.1 ± 0.3 ± 0.1	1.3 ± 0.2 ± 0.3
Other SM	0.3 ± 0.1 ± 0.1	0.5 ± 0.2 ± 0.2	0.9 ± 0.4 ± 0.1	0.2 ± 0.1 ± 0.1	2.0 ± 0.6 ± 0.3	1.2 ± 0.4 ± 0.2
Total prediction	2.1 ± 0.6 ± 0.6	5.5 ± 1.2 ± 1.7	6.2 ± 1.2 ± 2.2	4.9 ± 1.3 ± 0.5	22.5 ± 3.0 ± 9.5	23.9 ± 3.3 ± 6.0
Observed	5	1	5	7	19	26
$m(\widetilde{\tau}_L) = 100$ GeV	1.7 ± 0.2 ± 0.4	0.7 ± 0.2 ± 0.2	1.4 ± 0.2 ± 0.2	0.4 ± 0.1 ± 0.1	1.6 ± 0.2 ± 0.3	0.4 ± 0.1 ± 0.1
m_{T2} [GeV]	25 − 50					
Σm_T [GeV]	> 300		250 − 300		200 − 250	
N_j	0	≥ 1	0	≥ 1	0	≥ 1
Misidentified τ_h	2.8 ± 0.8 ± 1.8	0.5 ± 0.5 ± 0.2	3.1 ± 1.0 ± 1.7	3.6 ± 1.1 ± 2.0	23.5 ± 2.9 ± 9.8	12.7 ± 2.4 ± 4.2
DY+jets	< 0.7	1.5 ± 0.9 ± 0.5	0.4 ± 0.4 ± 0.1	1.6 ± 0.9 ± 0.3	4.3 ± 2.1 ± 0.7	4.5 ± 1.5 ± 0.9
Top quark	0.2 ± 0.1 ± 0.1	0.6 ± 0.2 ± 0.2	0.8 ± 0.2 ± 0.1	1.3 ± 0.2 ± 0.2	1.7 ± 0.3 ± 0.3	2.9 ± 0.4 ± 0.3
Other SM	0.3 ± 0.2 ± 0.1	0.9 ± 0.4 ± 0.2	0.7 ± 0.4 ± 0.1	1.2 ± 0.5 ± 0.3	2.4 ± 0.7 ± 0.4	0.5 ± 0.2 ± 0.1
Total prediction	3.2 ± 0.9 ± 1.8	3.5 ± 1.1 ± 0.6	5.1 ± 1.2 ± 1.7	7.7 ± 1.5 ± 2.1	31.9 ± 3.7 ± 9.8	20.6 ± 2.9 ± 4.3
Observed	3	3	5	4	28	25
$m(\widetilde{\tau}_L) = 100$ GeV	1.3 ± 0.2 ± 0.4	0.7 ± 0.2 ± 0.2	1.6 ± 0.2 ± 0.2	0.8 ± 0.2 ± 0.1	2.4 ± 0.3 ± 0.4	0.6 ± 0.2 ± 0.1

neutralino, significantly improving upon previous LHC limits.

Table 4: Predicted background yields and observed event counts in all $\tau_h\tau_h$ SRs, corresponding to $41.3\,\text{fb}^{-1}$ of data collected in 2017. For the background estimates with no events in the sideband or the simulated sample, the 68% statistical upper limit is taken. The uncertainties listed in quadrature are statistical and systematic respectively. We also list the predicted signal yields corresponding to the purely left-handed scenario for a $\widetilde{\tau}$ mass of $100\,\text{GeV}$ and a $\widetilde{\chi}_1^0$ mass of $1\,\text{GeV}$.

m_{T2} [GeV]	> 50					
Σm_T [GeV]	> 300		$250 - 300$		$200 - 250$	
N_j	0	≥ 1	0	≥ 1	0	≥ 1
Misidentified τ_h	$0.2 \pm 0.7 \pm 0.5$	$1.6 \pm 0.8 \pm 0.2$	$2.8 \pm 1.3 \pm 0.3$	$4.5 \pm 1.4 \pm 1.8$	$11.2 \pm 2.3 \pm 4.7$	$9.0 \pm 2.6 \pm 1.1$
DY+jets	< 0.7	$0.5 \pm 0.5 \pm 0.1$	$1.0 \pm 0.6 \pm 0.1$	$1.0 \pm 0.6 \pm 0.1$	$1.3 \pm 0.8 \pm 0.2$	$2.6 \pm 1.0 \pm 0.4$
Top quark	$0.4 \pm 0.3 \pm 0.1$	$0.6 \pm 0.5 \pm 0.2$	$0.3 \pm 0.3 \pm 0.1$	$0.1 \pm 0.1 \pm 0.0$	$0.8 \pm 0.4 \pm 0.1$	< 0.2
Other SM	$1.4 \pm 0.7 \pm 0.3$	$0.6 \pm 0.4 \pm 0.2$	$0.9 \pm 0.5 \pm 0.1$	$0.7 \pm 0.5 \pm 0.1$	$1.0 \pm 0.4 \pm 0.2$	$1.2 \pm 0.6 \pm 0.2$
Total prediction	$2.0 \pm 1.0 \pm 0.6$	$3.2 \pm 1.1 \pm 0.4$	$5.1 \pm 1.5 \pm 0.3$	$6.3 \pm 1.6 \pm 1.8$	$14.3 \pm 2.5 \pm 4.7$	$12.8 \pm 2.8 \pm 1.2$
Observed	3	3	7	9	11	24
$m(\widetilde{\tau}_L) = 100\,\text{GeV}$	$1.0 \pm 0.2 \pm 0.2$	$0.4 \pm 0.1 \pm 0.1$	$1.0 \pm 0.2 \pm 0.2$	$0.3 \pm 0.1 \pm 0.0$	$0.9 \pm 0.2 \pm 0.1$	$0.2 \pm 0.1 \pm 0.0$
m_{T2} [GeV]	$25 - 50$					
Σm_T [GeV]	> 300		$250 - 300$		$200 - 250$	
N_j	0	≥ 1	0	≥ 1	0	≥ 1
Misidentified τ_h	$0.5 \pm 0.5 \pm 0.1$	$1.9 \pm 0.8 \pm 1.3$	$2.7 \pm 0.9 \pm 1.0$	$1.1 \pm 0.8 \pm 0.3$	$18.6 \pm 3.1 \pm 3.6$	$9.4 \pm 2.1 \pm 1.7$
DY+jets	$1.1 \pm 0.8 \pm 0.3$	$1.0 \pm 0.8 \pm 0.1$	$1.9 \pm 1.4 \pm 0.5$	$0.6 \pm 0.4 \pm 0.2$	$5.0 \pm 2.0 \pm 0.7$	$1.5 \pm 0.7 \pm 0.2$
Top quark	$0.3 \pm 0.3 \pm 0.1$	$0.5 \pm 0.2 \pm 0.1$	$0.2 \pm 0.1 \pm 0.1$	$1.0 \pm 0.6 \pm 0.1$	$1.2 \pm 0.6 \pm 0.2$	$1.1 \pm 0.5 \pm 0.2$
Other SM	$0.5 \pm 0.3 \pm 0.1$	$0.6 \pm 0.4 \pm 0.3$	$0.7 \pm 0.5 \pm 0.1$	$0.5 \pm 0.5 \pm 0.1$	$1.9 \pm 0.7 \pm 0.4$	$1.4 \pm 0.6 \pm 0.4$
Total prediction	$2.4 \pm 1.0 \pm 0.4$	$4.0 \pm 1.2 \pm 1.4$	$5.5 \pm 1.8 \pm 1.1$	$3.2 \pm 1.2 \pm 0.4$	$26.7 \pm 3.8 \pm 3.7$	$13.3 \pm 2.3 \pm 1.8$
Observed	1	2	6	5	40	12
$m(\widetilde{\tau}_L) = 100\,\text{GeV}$	$1.4 \pm 0.2 \pm 0.4$	$0.6 \pm 0.1 \pm 0.2$	$1.3 \pm 0.2 \pm 0.2$	$0.3 \pm 0.1 \pm 0.0$	$1.7 \pm 0.2 \pm 0.2$	$0.4 \pm 0.1 \pm 0.1$

Table 5: Predicted background yields and observed event counts in the most sensitive last bins of the BDT distributions for each training, for the $e\tau_h$ and $\mu\tau_h$ final states, corresponding to $36.9\,\text{fb}^{-1}$ of data collected in 2016. The numbers in parentheses in the first row indicate the $\widetilde{\tau}$ and $\widetilde{\chi}_1^0$ masses corresponding to the signal model of left-handed $\widetilde{\tau}$ pair production used to train each BDT. In the last row, we list the predicted signal yields in the last bin of the BDT distribution for the same model.

BDT training	BDT($\mu\tau_h$,100,1)	BDT($\mu\tau_h$,150,1)	BDT($\mu\tau_h$,200,1)	BDT($e\tau_h$,100,1)	BDT($e\tau_h$,150,1)	BDT($e\tau_h$,200,1)
Misidentified τ_h	$1.6 \pm 0.8 \pm 0.3$	$2.3 \pm 1.0 \pm 0.4$	$1.5 \pm 0.8 \pm 0.3$	$3.3 \pm 1.1 \pm 0.5$	$0.2 \pm 0.4 \pm 0.1$	$0.5 \pm 0.7 \pm 0.3$
DY+jets	<0.1	$0.8 \pm 0.8 \pm 0.1$	<0.1	< 0.1	<0.1	$0.1 \pm 0.1 \pm 0.1$
Top quark	$0.3 \pm 0.3 \pm 0.1$	$1.8 \pm 1.2 \pm 0.2$	$1.7 \pm 1.2 \pm 0.6$	$0.2 \pm 0.2 \pm 0.1$	$0.2 \pm 0.2 \pm 0.1$	$1.4 \pm 0.8 \pm 2.0$
Other SM	$0.3 \pm 0.3 \pm 0.1$	$1.4 \pm 0.6 \pm 0.5$	$1.5 \pm 0.6 \pm 0.4$	$0.9 \pm 0.5 \pm 0.4$	$0.6 \pm 0.4 \pm 0.5$	$2.0 \pm 0.7 \pm 1.0$
Total prediction	$2.1 \pm 0.9 \pm 0.4$	$6.4 \pm 1.8 \pm 1.0$	$4.6 \pm 1.6 \pm 0.9$	$4.5 \pm 1.3 \pm 0.8$	$1.0 \pm 0.6 \pm 0.5$	$4.2 \pm 1.3 \pm 1.8$
Observed	1	6	7	5	2	7
Signal	$1.3 \pm 0.4 \pm 0.2$	$0.9 \pm 0.2 \pm 0.1$	$0.7 \pm 0.1 \pm 0.5$	$1.5 \pm 0.4 \pm 0.2$	$0.4 \pm 0.1 \pm 0.1$	$1.0 \pm 0.1 \pm 0.2$

Table 6: Predicted background yields and observed event counts in the most sensitive last bins of the BDT distributions for each training, for the $e\tau_h$ and $\mu\tau_h$ final states, corresponding to 41.3 fb^{-1} of data collected in 2017. The numbers in parentheses in the first row indicate the $\widetilde{\tau}$ and $\widetilde{\chi}_1^0$ masses corresponding to the signal model of left-handed $\widetilde{\tau}$ pair production used to train each BDT. In the last row, we list the predicted signal yields in the last bin of the BDT distribution for the same model.

| BDT training	BDT($\mu\tau_h$,100,1)	BDT($\mu\tau_h$,150,1)	BDT($\mu\tau_h$,200,1)	BDT($e\tau_h$,100,1)	BDT($e\tau_h$,150,1)	BDT($e\tau_h$,200,1)
Misidentified τ_h	$0.9 \pm 0.5 \pm 0.4$	<0.1	<0.1	$2.5 \pm 0.9 \pm 1.3$	$0.3 \pm 0.3 \pm 0.1$	<0.1
DY+jets	$2.1 \pm 2.1 \pm 3.3$	<0.1	<0.1	<0.1	<0.1	<0.1
Top quark	<0.1	$0.9 \pm 0.4 \pm 0.8$	$0.6 \pm 0.5 \pm 0.5$	$0.3 \pm 0.3 \pm 0.1$	<0.1	$0.2 \pm 0.2 \pm 0.2$
Other SM	<0.1	$1.0 \pm 0.7 \pm 1.6$	$0.6 \pm 0.6 \pm 1.1$	$1.0 \pm 0.7 \pm 1.5$	$0.2 \pm 0.2 \pm 0.5$	$1.0 \pm 0.6 \pm 1.6$
Total prediction	$3.0 \pm 2.2 \pm 3.1$	$2.0 \pm 1.0 \pm 2.0$	$1.2 \pm 0.7 \pm 1.3$	$3.7 \pm 1.1 \pm 2.3$	$0.4 \pm 0.4 \pm 0.5$	$1.2 \pm 0.7 \pm 1.6$
Observed	2	6	2	2	1	1
Signal	$0.6 \pm 0.3 \pm 0.1$	$0.4 \pm 0.1 \pm 0.8$	$0.6 \pm 0.1 \pm 0.3$	$1.0 \pm 0.4 \pm 0.1$	$0.2 \pm 0.1 \pm 0.1$	$0.2 \pm 0.1 \pm 0.1$
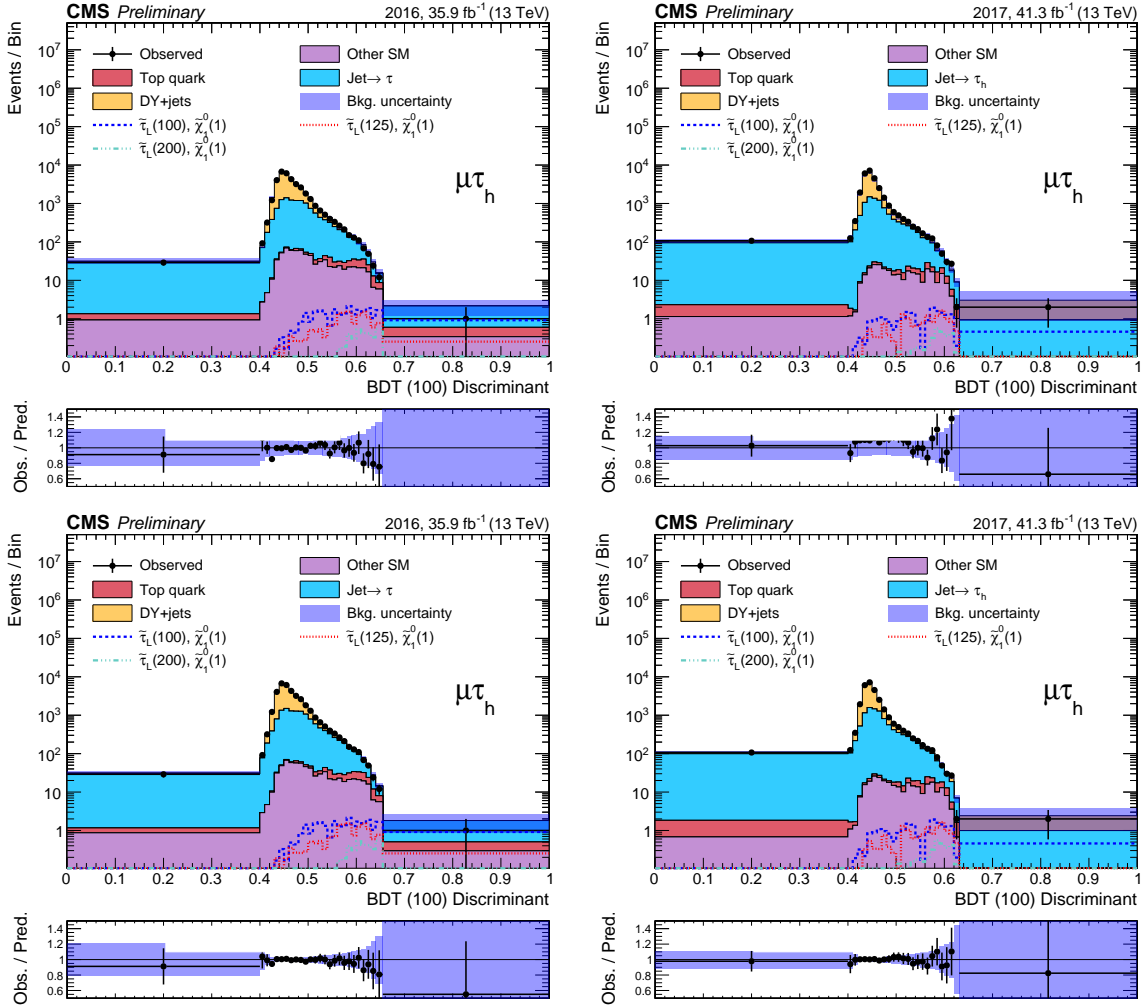
Figure 6: Distributions of the BDT discriminant for the BDT trained for a $\widetilde{\tau}$ mass of 100 GeV and a $\widetilde{\chi}_1^0$ mass of 1 GeV (BDT (100)) in the $\mu\tau_h$ final state for the 2016 (left) and 2017 (right) datasets, before (top) and after (bottom) the maximum likelihood fit to the data. Predicted signal yields are also shown for benchmark signal models with $m(\widetilde{\tau}) = 100, 125$, and 200 GeV, $m(\widetilde{\chi}_1^0) = 1$ GeV.
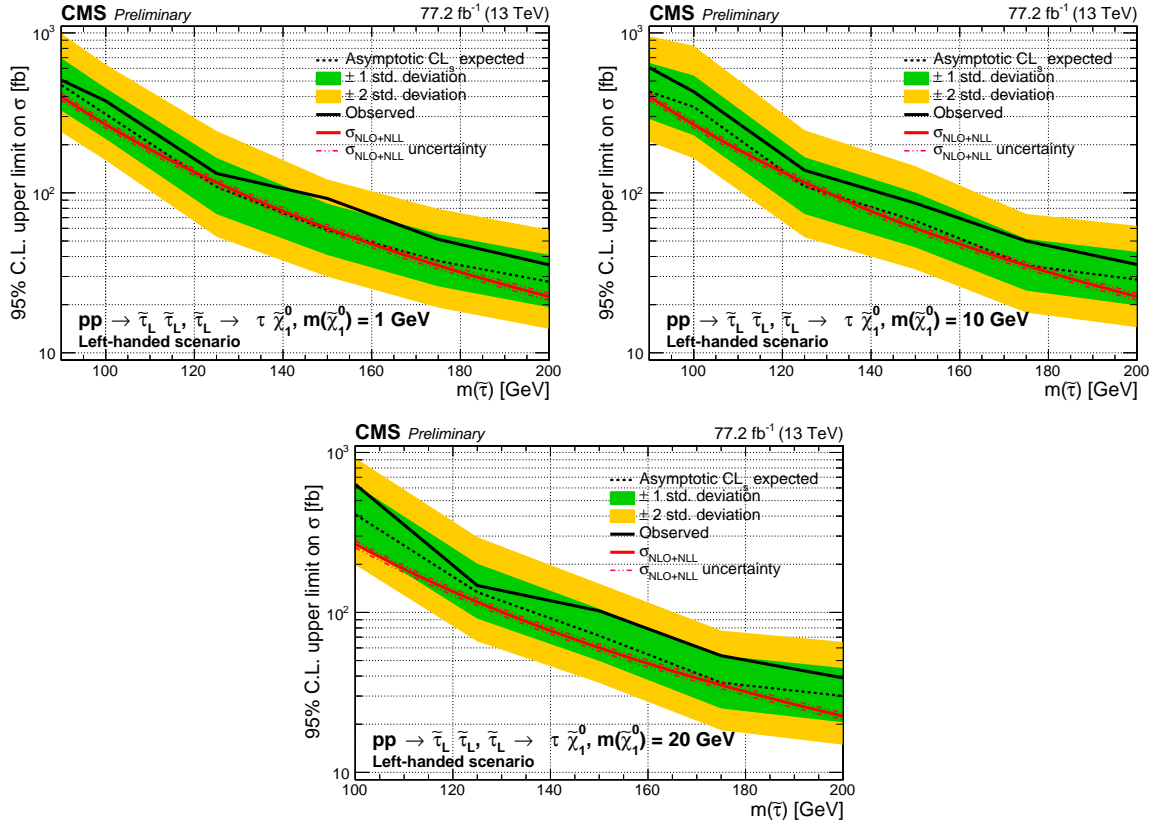
Figure 7: Cross section of $\widetilde{\tau}$ pair production excluded at 95% CL as a function of the $\widetilde{\tau}$ mass in the purely left-handed $\widetilde{\tau}$ scenario for a $\widetilde{\chi}_1^0$ mass of 1 (top left), 10 (top right) and 20 (bottom) GeV. The results shown are for the statistical combination of the 2016 and 2017 datasets for the $\tau_h\tau_h$ and $\ell\tau_h$ analyses. The inner (green) band and the outer (yellow) band indicate the regions containing 68 and 95%, respectively, of the distribution of limits expected under the background-only hypothesis. The red line indicates the NLO+NLL prediction for the signal production cross section calculated with RESUMMINO [35], while the red dashed lines represent the uncertainty in the prediction.
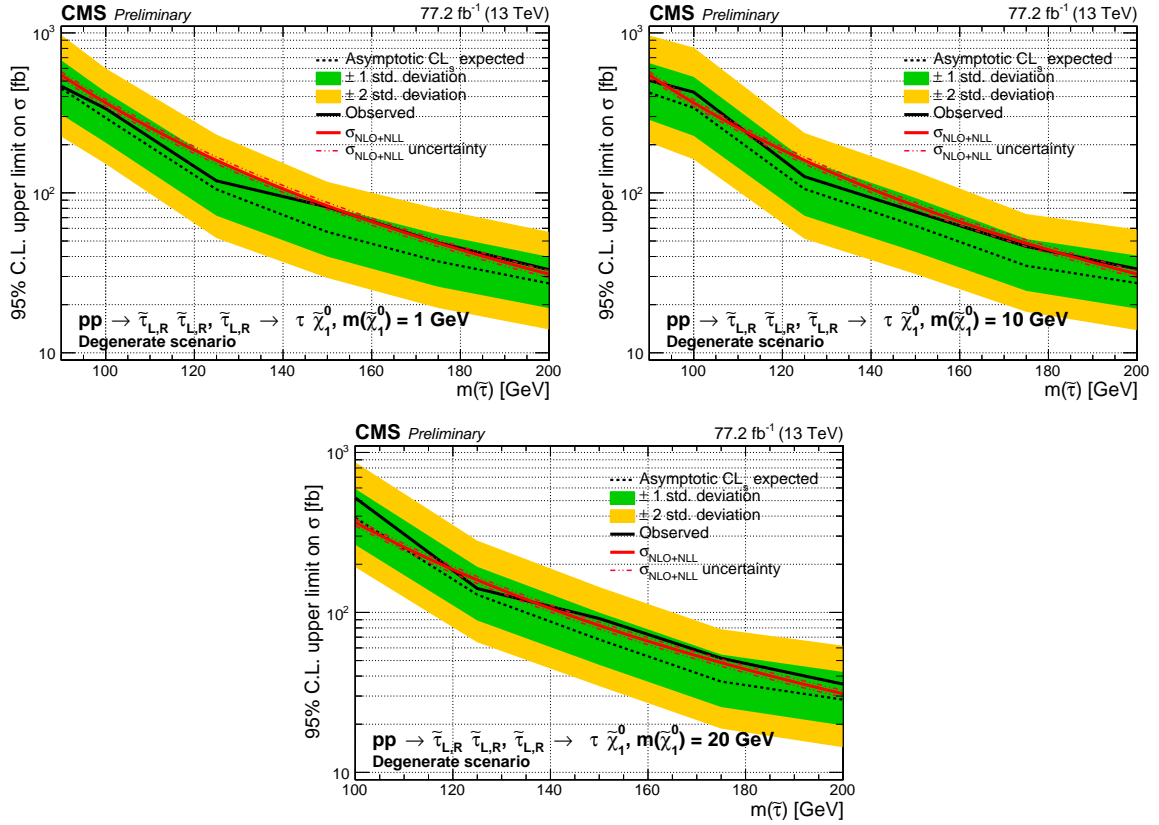
Figure 8: Cross section of $\tilde{\tau}$ pair production excluded at 95% CL as a function of the $\tilde{\tau}$ mass in the degenerate $\tilde{\tau}$ scenario for a $\tilde{\chi}_1^0$ mass of 1 (top left), 10 (top right) and 20 (bottom) GeV. The results shown are for the statistical combination of the 2016 and 2017 datasets for the $\tau_h\tau_h$ and $\ell\tau_h$ analyses. The inner (green) band and the outer (yellow) band indicate the regions containing 68 and 95%, respectively, of the distribution of limits expected under the background-only hypothesis. The red line indicates the NLO+NLL prediction for the signal production cross section calculated with RESUMMINO [35], while the red dashed lines represent the uncertainty in the prediction.

References

[1] P. Ramond, "Dual theory for free fermions", *Phys. Rev. D* **3** (1971) 2415, `doi:10.1103/PhysRevD.3.2415`.

[2] Y. A. Gol'fand and E. P. Likhtman, "Extension of the algebra of Poincaré group generators and violation of P invariance", *JETP Lett.* **13** (1971) 323.

[3] A. Neveu and J. H. Schwarz, "Factorizable dual model of pions", *Nucl. Phys. B* **31** (1971) 86, `doi:10.1016/0550-3213(71)90448-2`.

[4] D. V. Volkov and V. P. Akulov, "Possible universal neutrino interaction", *JETP Lett.* **16** (1972) 438.

[5] J. Wess and B. Zumino, "A Lagrangian model invariant under supergauge transformations", *Phys. Lett. B* **49** (1974) 52, `doi:10.1016/0370-2693(74)90578-4`.

[6] J. Wess and B. Zumino, "Supergauge transformations in four dimensions", *Nucl. Phys. B* **70** (1974) 39, `doi:10.1016/0550-3213(74)90355-1`.

[7] P. Fayet, "Supergauge invariant extension of the Higgs mechanism and a model for the electron and its neutrino", *Nucl. Phys. B* **90** (1975) 104, `doi:10.1016/0550-3213(75)90636-7`.

[8] H. P. Nilles, "Supersymmetry, supergravity and particle physics", *Phys. Rep.* **110** (1984) 1, `doi:10.1016/0370-1573(84)90008-5`.

[9] G. 't Hooft, "Naturalness, chiral symmetry, and spontaneous chiral symmetry breaking", *NATO Sci. Ser. B* **59** (1980) 135.

[10] E. Witten, "Dynamical breaking of supersymmetry", *Nucl. Phys. B* **188** (1981) 513, `doi:10.1016/0550-3213(81)90006-7`.

[11] M. Dine, W. Fischler, and M. Srednicki, "Supersymmetric technicolor", *Nucl. Phys. B* **189** (1981) 575, `doi:10.1016/0550-3213(81)90582-4`.

[12] S. Dimopoulos and S. Raby, "Supercolor", *Nucl. Phys. B* **192** (1981) 353, `doi:10.1016/0550-3213(81)90430-2`.

[13] S. Dimopoulos and H. Georgi, "Softly broken supersymmetry and SU(5)", *Nucl. Phys. B* **193** (1981) 150, `doi:10.1016/0550-3213(81)90522-8`.

[14] R. K. Kaul and P. Majumdar, "Cancellation of quadratically divergent mass corrections in globally supersymmetric spontaneously broken gauge theories", *Nucl. Phys. B* **199** (1982) 36, `doi:10.1016/0550-3213(82)90565-X`.

[15] C. Boehm, A. Djouadi, and M. Drees, "Light scalar top quarks and supersymmetric dark matter", *Phys. Rev. D* **62** (2000) 035012, `doi:10.1103/PhysRevD.62.035012`, `arXiv:hep-ph/9911496`.

[16] C. Balázs, M. Carena, and C. E. M. Wagner, "Dark matter, light stops and electroweak baryogenesis", *Phys. Rev. D* **70** (2004) 015007, `doi:10.1103/PhysRevD.70.015007`, `arXiv:hep-ph/403224`.

[17] G. R. Farrar and P. Fayet, "Phenomenology of the production, decay, and detection of new hadronic states associated with supersymmetry", *Phys. Lett. B* **76** (1978) 575, `doi:10.1016/0370-2693(78)90858-4`.

[18] G. Jungman, M. Kamionkowski, and K. Griest, "Supersymmetric dark matter", *Phys. Rept.* **267** (1996) 195, `doi:10.1016/0370-1573(95)00058-5`, `arXiv:hep-ph/9506380`.

[19] G. Hinshaw et al., "Nine-year Wilkinson Microwave Anisotropy Probe (WMAP) observations: cosmological parameter results", *Astrophys. J. Suppl.* **208** (2013) 19, `doi:10.1088/0067-0049/208/2/19`, `arXiv:1212.5226`.

[20] K. Griest and D. Seckel, "Three exceptions in the calculation of relic abundances", *Phys. Rev. D* **43** (1991) 3191, `doi:10.1103/PhysRevD.43.3191`.

[21] D. A. Vasquez, G. Belanger, and C. Boehm, "Revisiting light neutralino scenarios in the MSSM", *Phys. Rev. D* **84** (2011) 095015, `doi:10.1103/PhysRevD.84.095015`, `arXiv:1108.1338`.

[22] S. F. King, J. P. Roberts, and D. P. Roy, "Natural dark matter in SUSY GUTs with non-universal gaugino masses", *JHEP* **10** (2007) 106, `doi:10.1088/1126-6708/2007/10/106`, `arXiv:0705.4219`.

[23] M. Battaglia et al., "Proposed post-LEP benchmarks for supersymmetry", *Eur. Phys. J. C* **22** (2001) 535, `doi:10.1007/s100520100792`, `arXiv:hep-ph/0106204`.

[24] R. L. Arnowitt et al., "Determining the dark matter relic density in the minimal supergravity stau-neutralino coannihilation region at the Large Hadron Collider", *Phys. Rev. Lett.* **100** (2008) 231802, `doi:10.1103/PhysRevLett.100.231802`, `arXiv:0802.2968`.

[25] G. Belanger, S. Biswas, C. Boehm, and B. Mukhopadhyaya, "Light Neutralino Dark Matter in the MSSM and Its Implication for LHC Searches for Staus", *JHEP* **12** (2012) 076, `doi:10.1007/JHEP12(2012)076`, `arXiv:1206.5404`.

[26] E. Arganda, V. Martin-Lozano, A. D. Medina, and N. Mileo, "Potential discovery of staus through heavy Higgs boson decays at the LHC", *JHEP* **09** (2018) 056, `doi:10.1007/JHEP09(2018)056`, `arXiv:1804.10698`.

[27] J. Alwall, P. Schuster, and N. Toro, "Simplified models for a first characterization of new physics at the LHC", *Phys. Rev. D* **79** (2009) 075020, `doi:10.1103/PhysRevD.79.075020`.

[28] J. Alwall, M.-P. Le, M. Lisanti, and J. Wacker, "Model-independent jets plus missing energy searches", *Phys. Rev. D* **79** (2009) 015005, `doi:10.1103/PhysRevD.79.015005`.

[29] LHC New Physics Working Group, "Simplified models for LHC new physics searches", *J. Phys. G* **39** (2012) 105005, `doi:10.1088/0954-3899/39/10/105005`, `arXiv:1105.2838`.

[30] LEP SUSY Working Group (ALEPH, DELPHI, L3, OPAL), "Combined LEP selectron/smuon/stau results, 183-208 GeV", (2004). LEPSUSYWG/04-01.1.

[31] ATLAS Collaboration, "Search for the direct production of charginos, neutralinos and staus in final states with at least two hadronically decaying taus and missing transverse momentum in pp collisions at $\sqrt{s} = 8\,\text{TeV}$ with the ATLAS detector", *JHEP* **10** (2014) 96, `doi:10.1007/JHEP10(2014)096`, `arXiv:1407.0350`.

[32] ATLAS Collaboration, "Search for the electroweak production of supersymmetric particles in $\sqrt{s} = 8\,\text{TeV}$ pp collisions with the ATLAS detector", *Phys. Rev. D* **93** (2016) 052002, `doi:10.1103/PhysRevD.93.052002`, `arXiv:1509.07152`.

[33] CMS Collaboration, "Search for electroweak production of charginos in final states with two tau leptons in pp collisions at $\sqrt{s} = 8\,\text{TeV}$", *JHEP* **04** (2017) 018, `doi:10.1007/JHEP04(2017)018`, `arXiv:1610.04870`.

[34] CMS Collaboration, "Search for supersymmetry in events with a τ lepton pair and missing transverse momentum in proton-proton collisions at $\sqrt{s} = 13\,\text{TeV}$", *JHEP* **11** (2018) 151, `doi:10.1007/JHEP11(2018)151`, `arXiv:1807.02048`.

[35] B. Fuks, M. Klasen, D. R. Lamprea, and M. Rothering, "Revisiting slepton pair production at the Large Hadron Collider", *JHEP* **01** (2014) 168, `doi:10.1007/JHEP01(2014)168`, `arXiv:1310.2621`.

[36] CMS Collaboration, "Particle-flow reconstruction and global event description with the CMS detector", *JINST* **12** (2017) P10003, `doi:10.1088/1748-0221/12/10/P10003`, `arXiv:1706.04965`.

[37] CMS Collaboration, "Performance of missing transverse momentum reconstruction in proton-proton collisions at $\sqrt{s} = 13\,\text{TeV}$ using the CMS detector", `arXiv:1903.06078`.

[38] M. Cacciari, G. P. Salam, and G. Soyez, "The anti-k_T jet clustering algorithm", *JHEP* **04** (2008) 063, `doi:10.1088/1126-6708/2008/04/063`, `arXiv:0802.1189`.

[39] M. Cacciari, G. P. Salam, and G. Soyez, "FastJet user manual", *Eur. Phys. J. C* **72** (2012) 1896, `doi:10.1140/epjc/s10052-012-1896-2`, `arXiv:1111.6097`.

[40] CMS Collaboration, "Study of pileup removal algorithms for jets", CMS Physics Analysis Summary CMS-PAS-JME-14-001, 2014.

[41] CMS Collaboration, "Identification of b-quark jets with the CMS experiment", *JINST* **8** (2013) P04013, `doi:10.1088/1748-0221/8/04/P04013`, `arXiv:1211.4462`.

[42] CMS Collaboration, "Identification of heavy-flavour jets with the CMS detector in pp collisions at 13 TeV", *JINST* **13** (2018) P05011, `doi:10.1088/1748-0221/13/05/P05011`, `arXiv:1712.07158`.

[43] CMS Collaboration, "Performance of electron reconstruction and selection with the CMS detector in proton-proton collisions at $\sqrt{s} = 8\,\text{TeV}$", *JINST* **10** (2015) P06005, `doi:10.1088/1748-0221/10/06/P06005`, `arXiv:1502.02701`.

[44] CMS Collaboration, "Performance of the CMS muon detector and muon reconstruction with proton-proton collisions at $\sqrt{s} = 13\,\text{TeV}$", *JINST* **13** (2018) P06015, `doi:10.1088/1748-0221/13/06/P06015`, `arXiv:1804.04528`.

[45] CMS Collaboration, "Performance of reconstruction and identification of τ leptons decaying to hadrons and ν_τ in pp collisions at $\sqrt{s} = 13\,\text{TeV}$", *JINST* **13** (2018), no. 10, P10005, `doi:10.1088/1748-0221/13/10/P10005`, `arXiv:1809.02816`.

[46] J. Alwall et al., "The automated computation of tree-level and next-to-leading order differential cross sections, and their matching to parton shower simulations", *JHEP* **07** (2014) 079, `doi:10.1007/JHEP07(2014)079`, `arXiv:1405.0301`.

[47] P. Nason, "A new method for combining NLO QCD with shower Monte Carlo algorithms", *JHEP* **11** (2004) 040, `doi:10.1088/1126-6708/2004/11/040`, `arXiv:hep-ph/0409146`.

[48] S. Frixione, P. Nason, and C. Oleari, "Matching NLO QCD computations with Parton Shower simulations: the POWHEG method", *JHEP* **11** (2007) 070, `doi:10.1088/1126-6708/2007/11/070`, `arXiv:0709.2092`.

[49] S. Alioli, P. Nason, C. Oleari, and E. Re, "A general framework for implementing NLO calculations in shower Monte Carlo programs: the POWHEG BOX", *JHEP* **06** (2010) 043, `doi:10.1007/JHEP06(2010)043`, `arXiv:1002.2581`.

[50] E. Re, "Single-top *Wt*-channel production matched with parton showers using the POWHEG method", *Eur. Phys. J. C* **71** (2011) 1547, `doi:10.1140/epjc/s10052-011-1547-z`, `arXiv:1009.2450`.

[51] T. Sjöstrand et al., "An introduction to PYTHIA 8.2", *Comput. Phys. Commun.* **191** (2015) 159, `doi:10.1016/j.cpc.2015.01.024`, `arXiv:1410.3012`.

[52] GEANT4 Collaboration, "GEANT4 — a simulation toolkit", *Nucl. Instrum. Meth. A* **506** (2003) 250, `doi:10.1016/S0168-9002(03)01368-8`.

[53] A. Kalogeropoulos and J. Alwall, "The SysCalc code: A tool to derive theoretical systematic uncertainties", (2018). `arXiv:1801.08401`.

[54] NNPDF Collaboration, "Parton distributions for the LHC Run II", *JHEP* **04** (2015) 040, `doi:10.1007/JHEP04(2015)040`, `arXiv:1410.8849`.

[55] CMS Collaboration, "Search for top-squark pair production in the single-lepton final state in pp collisions at $\sqrt{s} = 8$ TeV", *Eur. Phys. J. C* **73** (2013) 2677, `doi:10.1140/epjc/s10052-013-2677-2`, `arXiv:1308.1586`.

[56] C. G. Lester and D. J. Summers, "Measuring masses of semiinvisibly decaying particles pair produced at hadron colliders", *Phys. Lett. B* **463** (1999) 99, `doi:10.1016/S0370-2693(99)00945-4`, `arXiv:hep-ph/9906349`.

[57] A. Barr, C. Lester, and P. Stephens, "m_{T2}: the truth behind the glamour", *J. Phys. G* **29** (2003) 2343, `doi:10.1088/0954-3899/29/10/304`, `arXiv:hep-ph/0304226`.

[58] C. G. Lester and B. Nachman, "Bisection-based asymmetric M_{T2} computation: a higher precision calculator than existing symmetric methods", *JHEP* **03** (2015) 100, `doi:10.1007/JHEP03(2015)100`, `arXiv:1411.4312`.

[59] D. Tovey, "On measuring the masses of pair-produced semi-invisibly decaying particles at hadron colliders", *JHEP* **04** (2008) 034, `doi:10.1088/1126-6708/2008/04/034`, `arXiv:0802.2879`.

[60] G. Polesello and D. Tovey, "Supersymmetric particle mass measurement with boost-corrected contransverse mass", *JHEP* **03** (2010) 030, `doi:10.1007/JHEP03(2010)030`, `arXiv:0910.0174`.

[61] C. Cuenca Almenar, "Search for the neutral MSSM Higgs bosons in the ditau decay channels at CDF Run II". PhD thesis, Valencia U., IFIC, 2008. `doi:10.2172/953708`.

[62] CMS Collaboration, "Search for neutral MSSM Higgs bosons decaying to a pair of tau leptons in pp collisions", *JHEP* **10** (2014) 160, `doi:10.1007/JHEP10(2014)160`, `arXiv:1408.3316`.

[63] CMS Collaboration, "Measurement of the differential Drell-Yan cross section in proton-proton collisions at $\sqrt{s} = 13$ TeV", *Submitted to: JHEP* (2018) `arXiv:1812.10529`.

[64] CMS Collaboration, "Measurements of $t\bar{t}$ differential cross sections in proton-proton collisions at $\sqrt{s} = 13$ TeV using events containing two leptons", *Submitted to: JHEP* (2018) `arXiv:1811.06625`.

[65] CMS Collaboration, "Measurement of the WW cross section pp collisions at sqrt(s)=13 TeV", CMS Physics Analysis Summary CMS-PAS-SMP-16-006, CERN, Geneva, 2016.

[66] CMS Collaboration, "CMS luminosity measurements for the 2016 data taking period", CMS Physics Analysis Summary CMS-PAS-LUM-17-001, 2017.

[67] CMS Collaboration, "CMS luminosity measurement for the 2017 data-taking period at $\sqrt{s} = 13$ TeV", Technical Report CMS-PAS-LUM-17-004, CERN, Geneva, 2018.

[68] CMS Collaboration, "Interpretation of searches for supersymmetry with simplified models", *Phys. Rev. D* **88** (2013) 052017, `doi:10.1103/PhysRevD.88.052017`, `arXiv:1301.2175`.

[69] T. Junk, "Confidence level computation for combining searches with small statistics", *Nucl. Instrum. Meth. A* **434** (1999) 435, `doi:10.1016/S0168-9002(99)00498-2`, `arXiv:hep-ex/9902006`.

[70] A. L. Read, "Presentation of search results: the CL$_s$ technique", *J. Phys. G* **28** (2002) 2693, `doi:10.1088/0954-3899/28/10/313`.

[71] The ATLAS Collaboration, The CMS Collaboration, The LHC Higgs Combination Group, "Procedure for the LHC Higgs boson search combination in Summer 2011", Technical Report CMS-NOTE-2011-005, ATL-PHYS-PUB-2011-11, 2011.

[72] G. Cowan, K. Cranmer, E. Gross, and O. Vitells, "Asymptotic formulae for likelihood-based tests of new physics", *Eur. Phys. J. C* **71** (2011) 1554, `doi:10.1140/epjc/s10052-011-1554-0`, `arXiv:1007.1727`. [Erratum: `doi:10.1140/epjc/s10052-013-2501-z`].